

Statistical Distortion of Supervised Learning Predictions in Optical Microscopy Induced by Image Compression

Enrico Pomarico (✉ enrico.pomarico@hesge.ch)

HEPIA, HES-SO, University of Applied Sciences and Arts Western Switzerland

Cédric Schmidt

HEPIA, HES-SO, University of Applied Sciences and Arts Western Switzerland

Florian Chays

HEPIA, HES-SO, University of Applied Sciences and Arts Western Switzerland

David Nguyen

École Polytechnique Fédérale de Lausanne

Arielle Planchette

École Polytechnique Fédérale de Lausanne

Audrey Tissot

Wyss Center for Bio and Neuroengineering

Adrien Roux

HEPIA, HES-SO, University of Applied Sciences and Arts Western Switzerland

Stéphane Pagès

Wyss Center for Bio and Neuroengineering

Laura Batti

Wyss Center for Bio and Neuroengineering

Christoph Clausen

Dotphoton SA

Theo Lasser

Max Planck Institute for Polymer Research

Aleksandra Radenovic

École Polytechnique Fédérale de Lausanne

Bruno Sanguinetti

Dotphoton SA

Jérôme Extermann

HEPIA, HES-SO, University of Applied Sciences and Arts Western Switzerland

Keywords: Statistical Distortion, Supervised Learning Predictions, Optical Microscopy, Image Compression

Posted Date: October 15th, 2021

DOI: <https://doi.org/10.21203/rs.3.rs-956884/v1>

License:  This work is licensed under a Creative Commons Attribution 4.0 International License.

[Read Full License](#)

Version of Record: A version of this preprint was published at Scientific Reports on March 2nd, 2022. See the published version at <https://doi.org/10.1038/s41598-022-07445-4>.

Statistical distortion of supervised learning predictions in optical microscopy induced by image compression

Enrico Pomarico^{1*}, Cédric Schmidt¹, Florian Chays¹, David Nguyen², Arielle Planchette², Audrey Tissot³, Adrien Roux¹, Stéphane Pagès^{3,4}, Laura Batti³, Christoph Clausen⁵, Theo Lasser⁶, Aleksandra Radenovic², Bruno Sanguinetti⁵, and Jérôme Extermann¹

¹ HEPIA, HES-SO, University of Applied Sciences and Arts Western Switzerland, Rue de la Prairie 4, 1202 Geneva, Switzerland

² Laboratoire de Biologie à l'Echelle Nanométrique, School of Engineering, École Polytechnique Fédérale de Lausanne, CH-1015 Lausanne, Switzerland

³ Wyss Center for Bio- and Neuroengineering, Geneva, Switzerland

⁴ Department of Basic Neurosciences, Geneva Neuroscience Center, Faculty of Medicine, University of Geneva, Geneva, Switzerland

⁵ Dotphoton SA, Zeughausgasse 17, 6300 Zug, Switzerland

⁶ Max-Planck Institute for Polymer Research, Ackermannweg 10, 55128 Mainz, Germany

*email: enrico.pomarico@hesge.ch

The growth of data throughput in optical microscopy has triggered the extensive use of supervised learning (SL) models on compressed datasets for automated analysis. Investigating the effects of image compression on SL predictions is therefore pivotal to assess their reliability, especially for clinical use.

We quantify the statistical distortions induced by compression through the comparison of predictions on compressed data to the raw predictive uncertainty, numerically estimated from the raw noise statistics measured via sensor calibration. Predictions on cell segmentation parameters are altered by up to 15% and more than 10 standard deviations after 16-to-8 bits pixel depth reduction and 10:1 JPEG compression. JPEG formats with higher compression ratios show significantly larger distortions. Interestingly, a recent metrologically accurate

algorithm, offering up to 10:1 compression ratio, provides a prediction spread equivalent to that stemming from raw noise. The method described here allows to set a lower bound to the predictive uncertainty of a SL task and can be generalized to determine the statistical distortions originated from a variety of processing pipelines in AI-assisted fields.

In the last years, an ever-growing community of optical microscopists is facing a massive data throughput, long-term storage costs, data transfer limitations and, more importantly, the need for automated quantitative data analysis, which has paved the way for extensive use of artificial intelligence (AI) methods. Supervised learning (SL) algorithms are routinely adopted to automate classification, segmentation, and artificial labelling of cellular or sub-cellular structures^{1,2,3}, biological tissues^{4,5,6}, as well as material defects^{7,8,9}. SL approaches have reported remarkable results in various fields, such as medical screening^{10,11}, single molecule localization^{12,13} and drug discovery^{14,15}. Deep-learning (DL) algorithms have also been successfully employed for micrograph restoration, in particular for de-noising and spatial resolution enhancement^{16,17,18}.

However, to deal with large training datasets and computational power constraints, SL models are ubiquitously executed on compressed imaging datasets. Despite producing visually faithful images, lossy compression algorithms are known to remove an unpredictable amount of information from the raw image. Moreover, compressed data often undergo additional processing before being used to train or test a SL model. Therefore, image compression can modify SL predictions with respect to when raw datasets are used and lead to unreliable scientific outcomes, based on how much the statistical distribution of the final predictions is altered. For this reason, the statistical distortions induced by compression need to be quantified to investigate the tolerability of image compression methods for SL applications.

To this end, it is crucial to measure the statistical distribution of the SL outcomes in the absence of compression, in other terms the prediction uncertainty associated to raw data. According to Begoli et al¹⁹, the lifecycle of an AI process from the physical sample to the AI-assisted decisions is affected by multiple sources of uncertainty. Understanding how image compression affects the statistical distribution of SL outcomes can be ascribed to investigating the representational uncertainty of the AI

pipeline, consisting in errors due to the data representation adopted for training or testing the SL model.

Here, we propose a method for quantifying the statistical distortions induced by compression in SL predictions. We first determine the predictive uncertainty in a SL-based optical microscopy application from the statistical noise of raw imaging data. Raw noise is measured via sensor calibration. As raw noise is unavoidable, our approach allows one to estimate the minimal level of representational uncertainty in SL predictions. Then, we compare outcomes obtained on compressed datasets to the raw predictive uncertainty by using a specific figure of merit, that will indicate the level of alteration of the SL outcomes statistics.

We implement this method to investigate the impact of image compression on the outcomes of cell segmentation tasks. To this end, we will consider three types of operations aimed at reducing data volume: pixel depth reduction, JPEG compression, as well as a metrologically accurate compression technique developed by the Dotphoton (DP) company (www.dotphoton.com). The DP method reports compression ratios from 5:1 to 10:1 after an initial image preparation step, in which image noise is replaced with a pseudo-random noise that closely mimics the statistical distribution of the raw pixel values. Although the noise replacement reduces the signal-to-noise ratio of each pixel by 1.2 dB, it allows to achieve high compression factors, as the pseudo-noise can be computed and makes the subsequent application of a standard lossless compression algorithm more efficient²⁰.

Results

Raw data statistical noise

Raw data, typically obtained through a digitization operation on a physical sample via an acquisition instrument, are intrinsically affected by the noise associated with the acquisition process. When an optical sensor is used, raw data variability is mainly provided by the quantum noise of the photons hitting the sensor, as well as by the electronic noise²¹. Hence, if one performs a sample acquisition under stabilized illumination conditions, as shown in Figure 1a, the acquired raw images are not identical and the raw pixel values display a statistical distribution of average μ and width σ (the standard deviation associated to the per-pixel noise).

Raw statistics could be in principle determined by repeating and averaging the acquisition of the same image several times. However, these tests are often hard to be carried out in a microscopy laboratory, because of sample variability, non-stationary illumination conditions, mechanical instabilities, as well as computational limitations.

Sensor calibration and measurement of statistical distortions of SL predictions

The first step of our method consists in calibrating the microscope's imaging sensor to determine an accurate mapping between light intensities and per-pixel noise. This is performed by sending to the sensor variable intensities from a homogeneous and controlled light source (see Supplementary Material).

Secondly, using the sensor-dependent calibration data (Figure 1b), statistically raw-equivalent images are numerically generated from a single raw image by replacing the original pixel value with a random one satisfying the raw pixel value statistical distribution (Figure 1c). By testing a previously trained SL model on the synthetic images (Figure 1e), the prediction spread σ_{raw} associated to a certain parameter χ can be determined similarly to a Monte-Carlo simulation.

As a final step, we evaluate whether image compression (Figure 1d) leads to predictions exceeding the original predictive uncertainty σ_{raw} . To this end, the difference between the values of a parameter χ without (χ_{raw}) and with compression (χ_c) is compared to σ_{raw} by using, as a figure of merit, the standard score defined as

$$\epsilon = \frac{\chi_{\text{raw}} - \chi_c}{\sigma_{\text{raw}}}.$$

A standard score ϵ such that $|\epsilon| < 1$ indicates that the statistical variability of SL predictions is smaller than that stemming from the natural noise of raw micrographs, defining therefore a general criterion for tolerability of statistical distortions induced by compression.

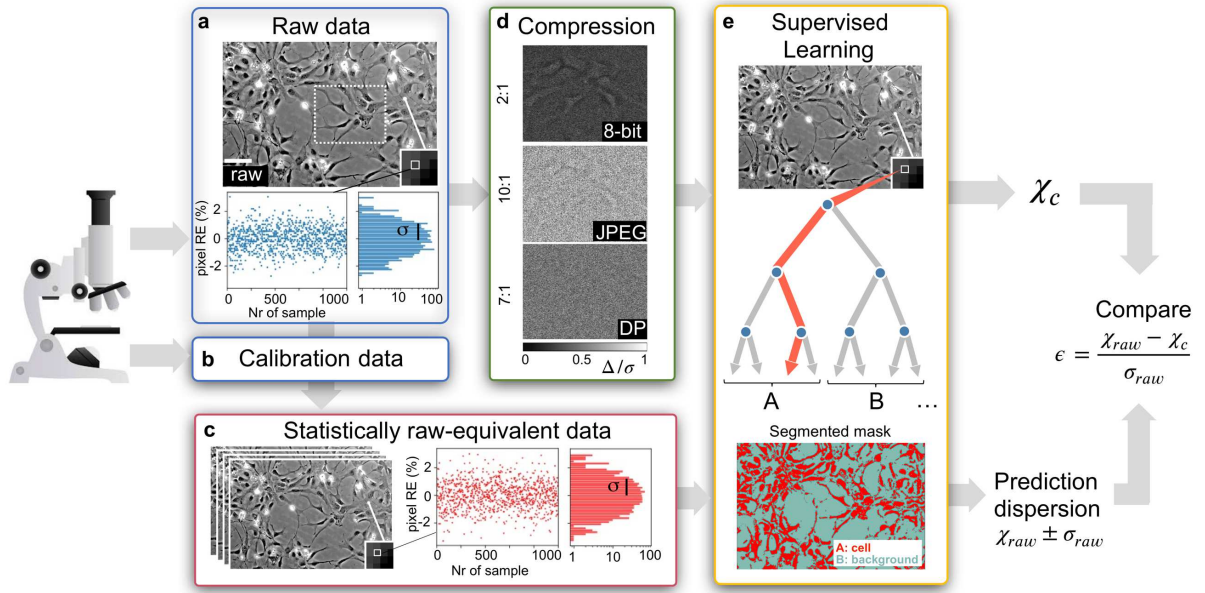


Figure 1 **Quantification of the statistical distortions induced by image compression on SL predictions**

2D cell segmentation

To demonstrate our method, we perform SL-based cellular segmentation tasks on 2-dimensional (2D) image datasets, obtained through phase-contrast (PC) microscopy, as well as 3-dimensional (3D) datasets obtained via light-sheet (LS) microscopy and optical projection tomography (OPT). By increasing the dimensionality of the raw dataset, we aim at observing how the complexification of raw data noise impacts the SL predictive uncertainty.

We first consider a cell segmentation task on PC images of microspheres, as well as mouse kidney collecting duct (MPK) cells. A random forest (RF) algorithm²², taking decisions on the basis of morphological spatial features, is trained via a manual pixel-based labelling performed on a raw image. After producing a segmentation map, we estimate parameters related to the whole image, as well as specific to single segmented objects. After calibration of the acquisition camera, we numerically generate a set of 10 statistically raw-equivalent images and determine the predictive uncertainty σ_{raw} of the considered parameters as the standard deviation of the values obtained with this dataset. The segmented mask obtained from an image of microspheres is shown in Figure 2a. In Figure 2d, we compare the total number of objects N_{tot} and the total segmented area A_{tot} predicted

from the raw image with those obtained from the corresponding 7:1 DP, 8-bit, 10:1 and 100:1 JPEG file. The difference in N_{tot} with respect to the raw value is in all cases less than 1% ($\epsilon \approx 1$). In contrast, the predicted value of A_{tot} in the 8-bit and JPEG cases ($\epsilon > 50$) shows a 2% deviation with respect to the raw result, while only 0.1% variation in the DP case ($\epsilon = -2$).

We then perform a similar analysis on 19 different morphological parameters estimated for each segmented object (area, coordinates of the center of mass (X_{CM} , Y_{CM}), perimeter, major axis, minor axis, ellipsoid angle, circularity, Feret, Feret X, Feret Y, Feret angle, Minimum Feret, aspect ratio, roundness, solidity, Feret aspect ratio, compactness, and extent)²³. The inset of Figure 2b shows a linear trend between the single-object area estimated from the raw (A_{raw}) and the DP (A_{DP}) mask. The groups of points accumulating along the diagonal correspond to aggregates of microspheres. The mean and the standard deviation of the distribution of the difference in the single-object area (ΔA) obtained from the synthetic raw-equivalent images with respect to the raw ones is in good agreement with the one obtained for the DP format. However, a clear shift of around 3 pixels and a larger spread of the distribution of ΔA is observed in the 8-bit and JPEG cases (Figure 2c and Table 1).

In Figure 2e, we plot the standard scores ϵ for all parameters averaged over all objects. All scores for the DP format are close to zero and have standard deviations (indicated by error bars) of the order of 1, showing that alterations induced by the DP compression can be considered statistically equivalent to those produced by the intrinsic noise of the raw images. In contrast, the distribution of the standard scores is larger than the $[-1,1]$ interval, in some cases of up to 10 standard deviations, with mean values far from 0 for almost all parameters in the 8-bit and JPEG cases. These results imply that predictions on the 8-bit and JPEG files exceed the predictive uncertainty provided by the raw statistical noise. Statistical distortions of predictions on JPEG files are similar to the 8-bit case when the 10:1 factor is used and deviate dramatically (more than 10 standard deviations for almost all parameters) from the raw ones as the compression ratio increases.

The same analysis is performed on a PC micrograph of MPK cells with high confluence and high mean pixel intensity (Figure 2f). In these experimental conditions, the good agreement between the DP and the raw results is confirmed. We observe a 1-2% deviation in the values of A_{tot} and N_{tot} in the 8-bit and 10:1 JPEG cases (Figure 2g). As concerns the single object parameters (Figure 2h), the

statistical equivalence of processing results on raw and DP data is confirmed despite the more complex cell spatial configuration. In contrast, predictions on single-object parameters are significantly altered in the 8-bit pixel depth and JPEG cases. This effect turns out to be more relevant for the MPK cells than for the microspheres image, probably because of the presence of larger spatial frequencies, such that more information is lost for the same compression ratio.

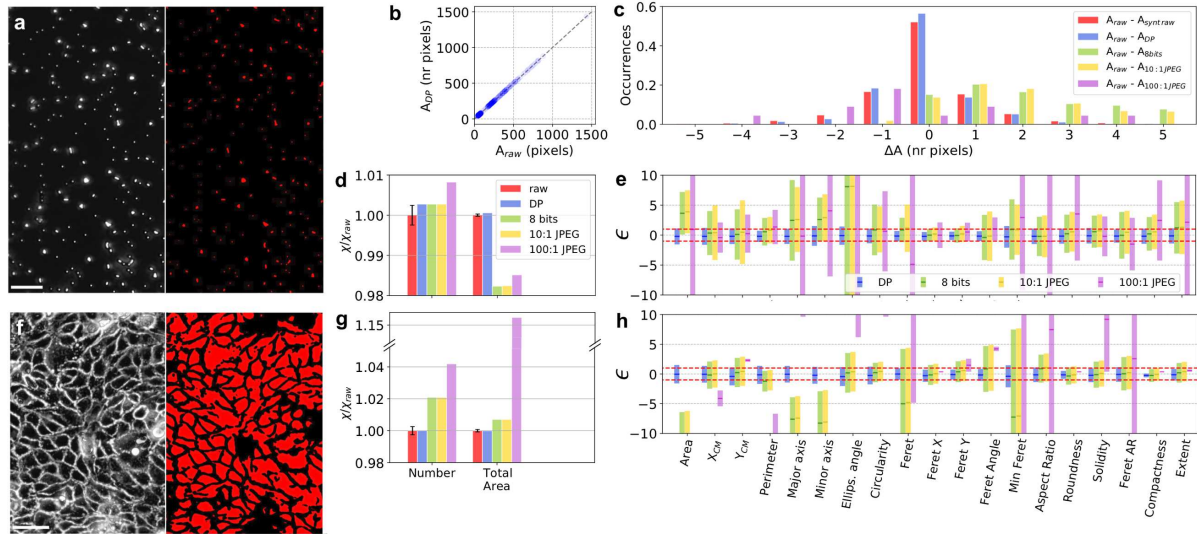


Figure 2 Statistical distortions induced by compression in 2D segmentation tasks in PC microscopy

	$\mu_{\Delta A}$ (nr pixels)	$\sigma_{\Delta A}$ (nr pixels)
Synthetic raw-equivalent images	0.1	1.1
DP	-0.1	1.0
8 bits	3.0	3.4
10:1 JPEG	3.1	3.4
100:1 JPEG	2.9	10.3

Table 1 Distribution of the difference in the area of the single objects segmented in the PC microspheres image with respect to the raw outcomes (Figure 2c)

3D cell segmentation

We then challenge our method on more complex segmentation tasks involving 3D datasets produced by LS microscopy and OPT.

By using of a RF voxel classification algorithm, we perform segmentation of neuronal nuclei in a portion of a mouse brain after *c-fos* antibody staining, imaged by a mesoscale Selective Plane Illumination LS Microscope (mesoSPIM) (Figure 3a, b, c)²⁴ and providing a 4.3 GB raw dataset. To obtain the 3D segmented volumes, a threshold criterion is applied to the 3D probability map obtained from the trained ML model. We perform these tests only with the DP method (7.3:1 compression ratio), and 8-bit down-sampling, as JPEG formats are not generally utilized in these fields.

As shown in Figure 3f, the number of segmented nuclei N_{tot} (around 190'000), as well as the total segmented volume V_{tot} and surface area SA_{tot} calculated from the DP dataset, display a discrepancy of 0.1-0.2% with respect to the values obtained from the raw segmented 3D image ($\epsilon = -1.6, -0.9, -0.1$ for N_{tot} , V_{tot} and SA_{tot} respectively) and are perfectly compatible with the spread shown by the synthetic images. In contrast, for all global parameters, the 8-bit conversion provides 15-20% discrepancy, much larger than in the 2D case ($\epsilon = 366, 87, 9$ for N_{tot} , V_{tot} and SA_{tot} respectively).

The 2D histogram in Figure 3d compares the volume in voxels of each single object identified in the raw (V_{raw}) and in the DP dataset (V_{DP}). To identify the same corresponding objects in the two datasets, especially those not having the same center coordinates after segmentation, an association based on the minimal Euclidean distance is performed. The accumulation of points along the diagonal of the histogram in Figure 3d reveals the agreement of the predictions obtained with the raw and the DP datasets. The distribution of single-volume differences ΔV with respect to the raw outcomes (Figure 3g and Table 2), obtained from the synthetic raw files is in good agreement with that provided by the DP stack. Interestingly, the 8-bit conversion alters the distribution of ΔV in a more dramatic way compared to the 2D case (Figure 3e), confirming the results obtained for the global parameters. The 8-bit conversion seems affecting the action of the morphological operators used in the SL algorithm in a more complex way with respect to the 2D case (Table 2). This effect is probably due to the higher noise correlation existing between the different slices of the 3D LS microscopy dataset.

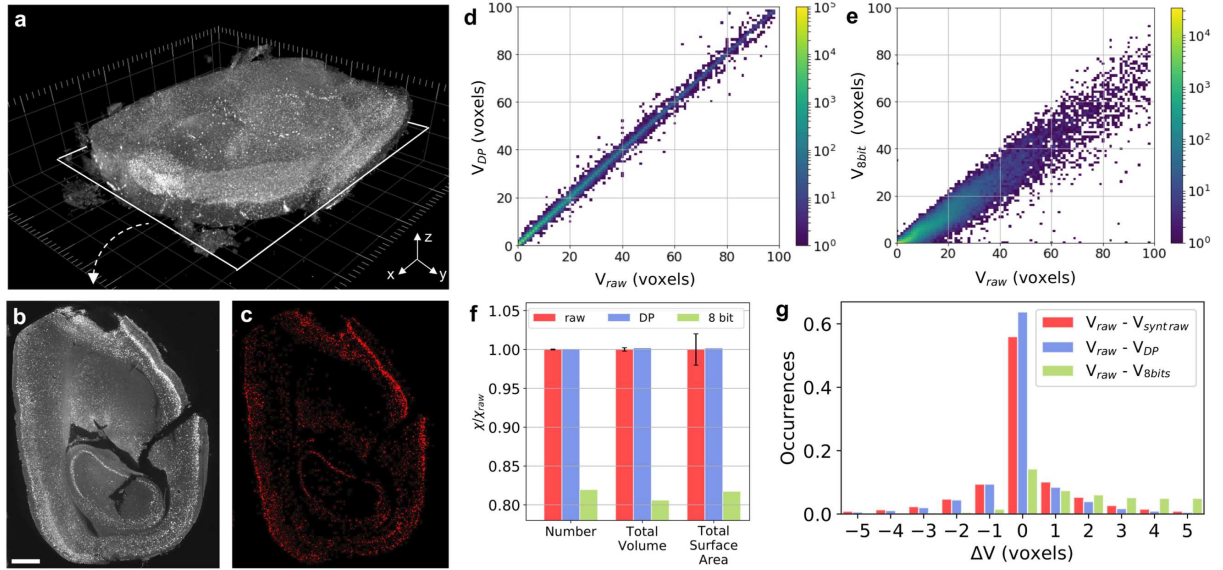


Figure 3 **Statistical distortions induced by compression in 3D segmentation tasks in light-sheet microscopy**

	$\mu_{\Delta V}$ (nr voxels)	$\sigma_{\Delta V}$ (nr voxels)
Synthetic raw-equivalent images	0.1	2.7
DP	-0.1	2.2
8 bits	7.3	6.4

Table 2 **Distribution of the difference in the volume of the single objects segmented in the LS 3D image with respect to the raw outcomes (Figure 3g)**

We then adopt our compression tolerability method on a pre-clinical application, based on the estimation of amyloidosis in a middle-aged mouse brain affected by Alzheimer's disease via Optical Projection Tomography (OPT) imaging. OPT is well suited to image mesoscopic centimeter-sized biological specimens, such as organs, and represents the optical equivalent of computed tomography: fluorescent projection images are captured at different angles around the specimen and the 3D image of the organ is reconstructed via a Filtered Back Projection (FBP) algorithm using an inverse Radon transform (Figure 4a, b, c)²⁵. Compared to the segmentation performed on LS microscopy data, an

image reconstruction step is introduced before the AI testing, making more complex the propagation of the original noise of the raw projections through the AI pipeline. To obtain the amyloid plaques segmentation mask on the raw and compressed 3D images, we adopt the same RF algorithm used for the LS microscopy data to classify every voxel of the reconstructed images and apply a threshold criterion on the 3D probability map (namely 0.7 for brain anatomy and 0.5 for amyloid plaques) according to a previous study²⁶. A close up of a slice of a reconstructed diseased mouse brain and the corresponding plaques segmentation mask are shown in Figure 4d and e, respectively. In this experiment, to quantify the SL predictive uncertainty, we simulate a dataset of 10 statistically raw-equivalent projections of the mouse brain.

The voxel classifier relies on intensity-based, edge-based, as well as texture operators, computed on the 3D image after various levels of Gaussian smoothing. We first compare the results of all operators on the raw dataset of 0.5 GB size, the 7.8:1 DP compressed and the 8-bit converted projections datasets, by calculating their standard scores averaged over all projection pixels. As shown by Figure 4f, the averaged standard scores belong for all parameters to the $[-1,1]$ interval in the DP case. In contrast, the 8-bit conversion shows in general larger discrepancies for an increasing gaussian smoothing. Similar results are found when the considered processing operations are performed after the 3D reconstruction (Figure 4g). In this case, the averaged standard scores of the gaussian smoothing operators applied over all voxels of the reconstructed 3D images are around 0 because smoothing is already performed in the applied FBP algorithm²⁶.

Finally, we compare the sensitivity of the quantitative analysis of amyloidosis in the mouse brain to DP compression and 8-bit conversion. Given the complete 3D prediction map, we compute the values of the standard scores for four plaque parameters: the total volume of plaque, the plaque load (the ratio of plaque volume to the total organ volume), the total plaque count and the plaque mean volume. The results, shown in Figure 4h, indicate that global segmentation parameters are conserved upon DP compression. In contrast, the 8-bit conversion provides around 5% deviation with respect to the raw values, confirming the alteration of the raw predictions also in this case.

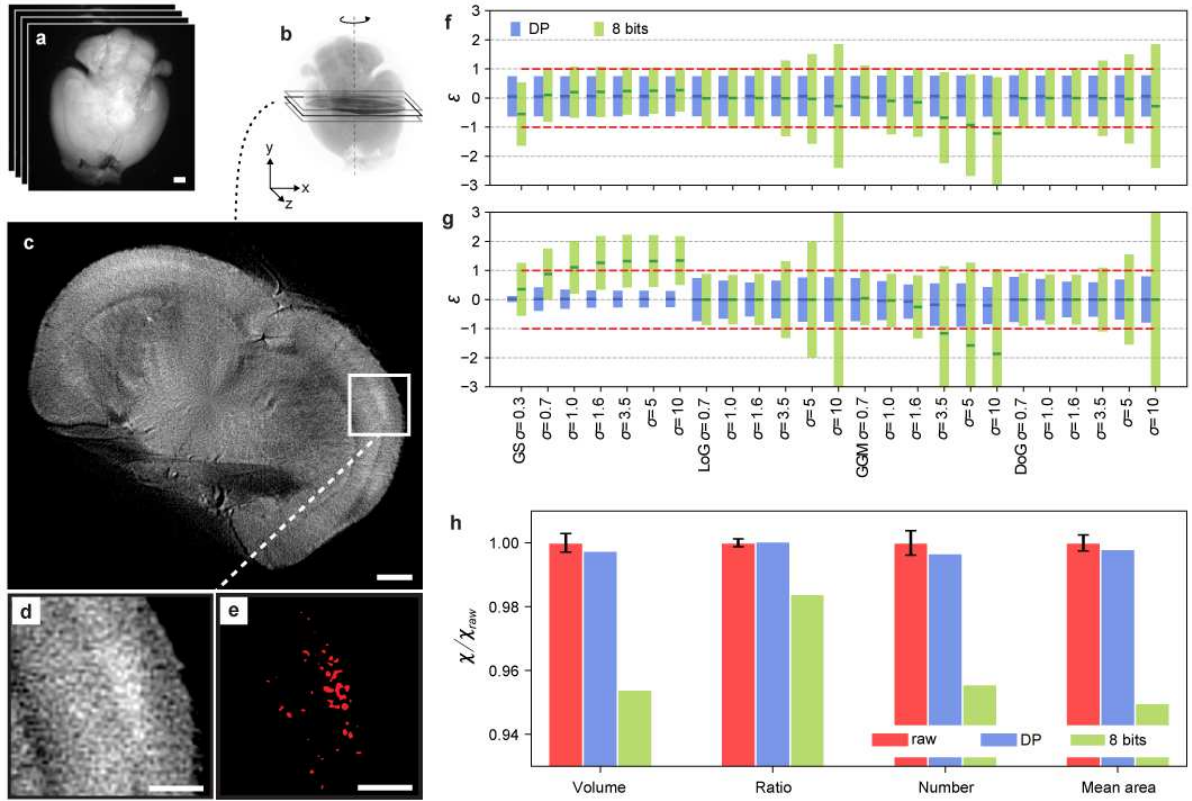


Figure 4 Statistical distortions induced by compression in 3D segmentation of amyloid Alzheimer plaques imaged via optical projection tomography

Discussion

In this work, we show the statistical nature of the distortions induced by image compression on the outcomes of SL tasks in optical microscopy. We present an experimental method capable of quantifying these statistical distortions, relying on determining the SL predictive uncertainty from the intrinsic statistical noise of raw data. As raw noise is unavoidable, our approach sets a lower bound to the predictive uncertainty in SL-assisted decision-making processes.

We show that 16-to-8 bits pixel depth reduction and JPEG compression can alter SL outcomes by more than 10 standard deviations. Interestingly, these distortions are more relevant in 3D applications: the use of 8-bit conversion brings to 5% and 15% prediction change in OPT and LS datasets segmentation, respectively, exceeding raw predictions by many standard deviations. The different distortions in the two 3D cases are probably related to the different propagation of the raw data noise through the processing pipeline. In contrast, we observe that alterations induced by the DP

compression can be considered as statistically equivalent to those provided by the raw noise in both 2D and 3D cases. By respecting the raw pixel value statistics and providing compressed images with size reduced by a factor up to 10, the DP image format represents a valuable solution to computational and data management challenges associated to computer-vision automated tasks in microscopy.

In this work, we also measure the statistical distortions of the predictions of a pre-clinical cell segmentation task in OPT. Our results indicate that the reliability of scientific outcomes obtained in diagnostic applications can be compromised by image compression in a non-negligible way. Finally, our work highlights the importance to preserve raw pixel value statistics in image processing pipelines to achieve the minimum prediction spread for an AI model. We expect our method to be generalizable to any field where acquisition devices can be calibrated and raw data are processed before AI use.

Figure legends

Figure 1 **Quantification of the statistical distortions induced by image compression on SL predictions**

a Raw imaging data from a microscope are intrinsically affected by noise: pixel values in a raw micrograph (in the figure a PC image of human neural stem cells (scale bar: 100 μm)) have a statistical distribution of width σ and mean μ . This is shown by the plot of the relative error (RE) of the single pixel values obtained from 1000 acquired images at the corresponding light intensity (insets). **b, c** Via calibration data of the acquisition sensor, statistically raw-equivalent unprocessed images (with same σ and μ) are generated. **d** Image compression is performed on raw data: the differences between the 8-bit, 10:1 JPEG, 7:1 DP compressed formats and the raw image (Δ), normalized to the per-pixel noise σ (Δ/σ), indicate the artifacts induced by compression on the original image. The displayed image portions correspond to the dotted rectangle in **a**. **e** A pre-trained SL model (based in our work on a Random Forest algorithm), producing cell segmentation masks, is tested on the statistically raw-equivalent synthetic data to determine the standard deviation σ_{raw} associated to a certain parameter χ_{raw} . The model also predicts a value of the considered parameter from the compressed data χ_{c} . To verify the statistical impact of image compression, the value of χ_{c} is compared to χ_{raw} via the standard score $\epsilon = \frac{\chi_{\text{raw}} - \chi_{\text{c}}}{\sigma_{\text{raw}}}$. If $|\epsilon| > 1$, SL predictions on the compressed image exceed the statistical variability stemming from raw data noise.

Figure 2 **Statistical distortions induced by compression in 2D segmentation tasks in PC microscopy**

a Micrograph of microspheres (scale bar: 20 μm) with corresponding segmentation mask. **b** Area of each segmented object obtained from the raw (A_{raw}) and the corresponding 6.7:1 DP compressed image (A_{DP}) for all objects. **c** Histogram of the difference in the single object area (ΔA) determined from the raw and the statistically raw-equivalent images ($A_{\text{raw}} - A_{\text{synt raw}}$), the DP ($A_{\text{raw}} - A_{\text{DP}}$), the 8-bit

($A_{\text{raw}} - A_{\text{8bit}}$), the 10:1 JPEG ($A_{\text{raw}} - A_{10:1 \text{ JPEG}}$) and the 100:1 JPEG file ($A_{\text{raw}} - A_{100:1 \text{ JPEG}}$). **d** Values of the parameters associated to the whole segmented image, such as number of objects and total segmented area, obtained from the DP, the 8-bit and the JPEG segmented images and normalized to the raw value. The error bars on the raw values are calculated from the standard deviation of the values obtained from the synthetic raw images. **e** Average of the standard score ϵ of 19 parameters associated to the single segmented objects. **f** PC Micrograph of MPK cells (scale bar: 50 μm) with segmentation mask, down-sampled to 8-bits and compressed into 6.1:1 DP, 10:1 and 100:1 JPEG formats. **g, h** Same as **d** and **e** for the MPK cells.

Figure 3 Statistical distortions induced by compression in 3D segmentation tasks in light-sheet microscopy

a 3D light-sheet image composed of 550 slices from a portion of a mouse brain obtained after *c-fos* staining performed to identify neuronal nuclei (1 voxel = 5.26 μm x 5.26 μm x 5 μm = 138 μm^3). **b** Single slice of the 3D image (scale bar: 1 mm) **c** Corresponding segmentation mask. **d, e** 2D histogram comparing the volume of the same objects in the raw (V_{raw}) and the 7.3:1 DP 3D compressed image (V_{DP}) (**d**), as well as the 8-bit 3D image ($V_{\text{8 bits}}$) (**e**). **f** Values of the parameters associated to the whole segmented image, such as the number of objects, total segmented volume and surface area, obtained from the DP and 8-bit segmented image, normalized to the raw value. The error bars on the raw values are calculated from the standard deviation of the values obtained from the synthetic 3D images. **g** Histogram of the difference in the single object volume (ΔV) calculated from the raw and the statistically raw-equivalent images ($V_{\text{raw}} - V_{\text{synt raw}}$), the DP ($V_{\text{raw}} - V_{\text{DP}}$), and the 8-bit 3D image ($V_{\text{raw}} - V_{\text{8bit}}$).

Figure 4 Statistical distortions induced by compression in 3D segmentation of amyloid Alzheimer plaques imaged via optical projection tomography

a-c Typical OPT pipeline. Fluorescent projections of an organ at different angles are used to reconstruct its 3D image via an inverse Radon transform. Transverse slices are used for physiological

analysis (scale bar: 1 mm). **d** Close-up of a reconstructed slice showing amyloid plaque deposition in the mice brain. **e** Segmented mask of amyloid plaques (scale bar: 300 μm). **f, g** Plot of the single pixel standard scores of four image-processing operators for different sizes of the Gaussian-smoothing kernel calculated on projections (**f**) and reconstructed slices (**g**) obtained from the 7.8:1 DP compressed and the 8-bit converted 3D image. **h** Normalized values of amyloid plaque characteristics associated to the whole dataset, obtained from the raw (red), the DP compressed (blue) and the 8-bit converted datasets (green). The error bars on the raw values are determined via the synthetic statistically raw-equivalent 3D images.

Acknowledgements

The authors are grateful to Eric Feraille from University of Geneva for providing the mpkCCDC14 (MPK) cell samples, as well as F. Bugnon and C. Brack for technical support. This project has been partially funded by Innosuisse (grant no 31434.1 IP-ICT) and by the Horizon 2020 Framework Programme of the European Union with the project ADgut (grant no 686271).

Authors contribution

E. P. performed PC and LS segmentation analysis. C. S. performed OPT segmentation analysis. F. C. acquired PC images. D. N. and A. P. prepared samples and performed OPT measurements. A. T. prepared samples for LS microscopy. A. Ro. prepared samples for PC measurements. S. P. and L. B. provided LS datasets and contributed to LS microscopy data analysis. C.C. supported in the use of DP compression. T. L. co-designed the OPT system. T. L. and A. Ra. contributed to the idea of the paper and supervised the OPT data acquisition. B. S. contributed to the idea of the paper and in writing the article. E. P. and J. E. conceived the presented idea. J. E. supervised the project. E. P., C. S. and J. E. wrote the article.

Competing interests

C. C. and B. S. are founding members of the company Dotphoton SA commercializing image compression solutions.

Methods

PC

For PC microscopy measurements, we used two inverted PC microscopes (Axiovert 40C and Axiovert 25, Carl Zeiss Jena GmbH) equipped with 5x, 10x and 20x objectives and a calibrated CMOS camera (CM3-U3-31S4M-CS, Sony). Samples of carboxylate microspheres of 500 nm diameter (Polysciences) were obtained by depositing 5 μ L of an aqueous solution with a concentration of $3.6 \cdot 10^8$ particles/mL on a 170 μ m thick glass slide. After solvent evaporation, PMMA at 0.1g/mL was added to the sample, then centrifugated and dried. Microspheres were imaged with a 20x objective and used for segmentation tests, as well as for the measurement of the microscope's point spread function (PSF). Two cell lines with variable confluence have been cultured: human neural stem cells (HIP) (A3890101, ThermoFisher)²⁷ and mpkCCDC14 mouse kidney collecting duct cells (MPK)^{28,29}. Both cell lines were cultured and grown on a cell treated plastic surface at a temperature of 37 °C with an air atmosphere enriched with 5% CO₂. Micrographs of HIP and MPK cells were obtained with a 10x and 20x objective, respectively. For the measurement of the modulation transfer function (MTF), we imaged the 1951 USAF test target (R3L3S1P, Thorlabs Inc.) in bright field configuration with the 5x objective.

All segmentation tests on PC images were carried out via the trainable Weka segmentation ImageJ plug-in³⁰, using a RF algorithm that produces pixel-based segmentations via a classification performed through the following training features: gaussian blur, hessian, sobel filter and difference of gaussians. To analyze the segmented masks, we used the "Extended Particle Analyzer" macro of the Biovoxxel toolbox in ImageJ²³, allowing to analyze the segmented objects according to a large variety of morphological parameters, shape descriptors and angle orientations. As the RF model was trained on a single 16-bit raw image, the synthetic images and the DP compressed were automatically suited to be tested by the model, while the 8-bit and JPEG files needed to be upsampled to 16-bit depth.

LS

For LS microscopy measurements, we used a home-built mesoscale single-plane illumination microscope²⁴. This setup consists of a dual-sided excitation path using a fiber-coupled multiline laser combiner (405, 488, 561 and 647 nm, Toptica MLE) and a detection path comprising a 42 Olympus MVX-10 zoom microscope with a 1x objective (Olympus MVPLAPO 1x), a filter wheel (Ludl 96A350), and a calibrated scientific CMOS camera (Hamamatsu Orca Flash 4.0 V3). The excitation paths also contain galvo scanners for light-sheet generation and reduction of shadow artifacts due to absorption of the light-sheet. In addition, the beam waist is scanned using electrically tunable lenses (ETL, Optotune EL-16-40-5D-TC-L) synchronized with the rolling shutter of the camera. Sample was illuminated by one of the two acquisition paths. Image acquisition was done using custom software written in Python 3. Z-stacks were acquired at 5 μm spacing with a zoom set at 1.25X resulting in an in-plane pixel size of 5.26 μm (2048x2048 pixels). Excitation wavelength of the *c-fos* antibody was set at 647 nm with an emission filter LP 663 nm bandpass filter (BrightLine HC, AHF). Concerning the sample preparation, mice were perfused with 4% PFA and tissue was post-fixed overnight in 4% PFA. Mouse brain were prepared for imaging following the iDISCO procedure described by Renier et al.³¹. To visualize a reporter of neuronal activity (*c-fos*), a *c-fos* antibody (synaptic System Anti *c-Fos* CN226003) was used to label the brain 1:2000 (0.25 $\mu\text{g}/\text{ml}$). This was coupled to an anti-rabbit Alexa Fluor-647 (far-red spectrum) (5 $\mu\text{g}/\text{ml}$). After clearing, brains were immersed in a 10 x 20 x 45 mm quartz cuvette filled with DiBenzyl Ether (RI 1.56).

For PSF measurements, fluorescent Tetraspeck microspheres 0.1 μm were diluted into 1% agarose. Excitation wavelength was set at 488 nm with an emission 530/40 nm bandpass filter (BrightLine HC, AHF).

The 3D segmentation tests on *c-fos* positive neuron nuclei were performed via a voxel classification workflow realized via the open-source image analysis software iLastik³². The training step consisted of a manual attribution of classes (anatomy, *c-fos* positive nuclei, background) to a few voxels of a reduced 3D volume. The trained algorithm could therefore predict the type of the remaining voxels in the full volume. To do so, the software attributed to each voxel a vector of features computed by typical image analysis operators and used RF as learning algorithm, where several decision trees were

built by randomly picking computed features and searching for proper decision boundaries to separate between classes. The output was a 3D probability map where the value of each voxel corresponded to the likelihood to be a *c-fos* positive neuronal nucleus. The final nuclei segmentation was then realized by applying a threshold value of 0.5 to the 3D probability map. As done for the 2D segmentation tests, the RF model was trained on a single 16-bit raw image stack, while the 8-bit stacks are upsampled to 16-bit depth.

OPT

For OPT measurements, we processed datasets of full intact mouse brains previously studied in ²⁶ using an SL approach to quantify amyloidosis of an Alzheimer's disease mouse model. The epifluorescent image projections were acquired with a custom mesoscopic OPT setup consisting of a calibrated CMOS camera (ORCA-Flash 4.0 V2, Hamamatsu) coupled to a 300-mm achromat objective lens providing 0.5X magnification of the sample³³. The sample was mounted on a motorized rotation stage allowing for projection acquisitions over 360 degrees by steps of 0.3 or 0.9 degrees in approximately five minutes. The sample fluorescent signal was excited by a 420-nm LED light source illuminating the whole organ. In this configuration, the OPT setup had an isotropic pixel-limited resolution of approximately 50 μm over the whole organ, due to the physical pixel size of the camera. Each set of projections (1024x1024x1200 matrix for 1200 projections) were previously saved as uncompressed 16-bit stacked .tif files. The 3D reconstruction of the sample was achieved by applying a filtered back-projection (FBP)³⁴ to the raw and compressed projection sets with the Matlab iRadon function. To do so, we follow the same procedure as previously described in ³³. After reconstruction, the 3D image volumes were cropped along the three dimensions in order to remove background contribution and conserve the brain signal only. The intensity of each voxels was normalized over the volume using Fiji³⁵ and its contrast enhancement tool before SL segmentation to accommodate for differences in dynamic range.

The plaque segmentation process relied on the same voxel classification workflow used for the segmentation of *c-fos* positive neuronal nuclei realized with the software iLastik³² on LS datasets. In this case, the three classes manually labeled in the training step were plaque, anatomy, and

background. 12 slices (2D) from the full mouse brain were manually annotated (brain tissues and amyloid plaques), half of them were used to train the RF algorithm, while the other half served as a test set. The final plaque segmentation and quantification was then realized by applying a threshold value of 0.5 to the 3D plaque probability map. This pipeline was the same as that provided by the authors of a previous study²⁶.

References

1. Sommer, C. & Gerlich, D. W. Machine learning in cell biology-teaching computers to recognize phenotypes. *J. Cell Sci.* **126**, 5529–5539 (2013).
2. Van Valen, D. A. *et al.* Deep Learning Automates the Quantitative Analysis of Individual Cells in Live-Cell Imaging Experiments. *PLoS Comput. Biol.* **12**, e1005177 (2016).
3. von Chamier, L., Laine, R. F. & Henriques, R. Artificial intelligence for microscopy: What you should know. *Biochem. Soc. Trans.* **47**, 1029–1040 (2019).
4. Vu, Q. D. *et al.* Methods for segmentation and classification of digital microscopy tissue images. *Front. Bioeng. Biotechnol.* **7**, 53 (2019).
5. Bychkov, D. *et al.* Deep learning based tissue analysis predicts outcome in colorectal cancer. *Sci. Rep.* **8**, 3395 (2018).
6. Xu, Y. *et al.* Large scale tissue histopathology image classification, segmentation, and visualization via deep convolutional activation features. *BMC Bioinformatics* **18**, 281 (2017).
7. Laanait, N., Zhang, Z. & Schlepütz, C. M. Imaging nanoscale lattice variations by machine learning of x-ray diffraction microscopy data. *Nanotechnology* **27**, 374002 (2016).
8. Bulgarevich, D. S., Tsukamoto, S., Kasuya, T., Demura, M. & Watanabe, M. Pattern recognition with machine learning on optical microscopy images of typical metallurgical microstructures. *Sci. Rep.* **8**, 2078 (2018).
9. Maksov, A. *et al.* Deep learning analysis of defect and phase evolution during electron beam-induced transformations in WS₂. *npj Comput. Mater.* **5**, 12 (2019).
10. Esteva, A. *et al.* Dermatologist-level classification of skin cancer with deep neural networks.

- Nature* **542**, 115–118 (2017).
11. Munir, K., Elahi, H., Ayub, A., Frezza, F. & Rizzi, A. Cancer diagnosis using deep learning: A bibliographic review. *Cancers (Basel)*. **11**, 1235 (2019).
 12. Zelger, P. *et al.* Three-dimensional localization microscopy using deep learning. *Opt. Express* **26**, 33166–33179 (2018).
 13. Möckl, L., Roy, A. R. & Moerner, W. E. Deep learning in single-molecule microscopy: fundamentals, caveats, and recent developments [Invited]. *Biomed. Opt. Express* **11**, 1633–1661 (2020).
 14. Chen, H., Engkvist, O., Wang, Y., Olivecrona, M. & Blaschke, T. The rise of deep learning in drug discovery. *Drug Discov. Today* **23**, 1241–1250 (2018).
 15. Stokes, J. M. *et al.* A Deep Learning Approach to Antibiotic Discovery. *Cell* **180**, 688–702 (2020).
 16. Rivenson, Y. *et al.* Deep learning microscopy. *Optica* **4**, 1437–1443 (2017).
 17. Wang, H. *et al.* Deep learning enables cross-modality super-resolution in fluorescence microscopy. *Nat. Methods* **16**, 103–110 (2019).
 18. Wu, Y. *et al.* Three-dimensional virtual refocusing of fluorescence microscopy images using deep learning. *Nat. Methods* **16**, 1323–1331 (2019).
 19. Begoli, E., Bhattacharya, T. & Kusnezov, D. The need for uncertainty quantification in machine-assisted medical decision making. *Nat. Mach. Intell.* **1**, 20–23 (2019).
 20. Sanguinetti, B. & Clausen, C. Method and device for steganographic processing and compression of image data. US Patent App. 17/090,577 (2020).
 21. Pence, W. D., Seaman, R. & White, R. L. Lossless Astronomical Image Compression and the Effects of Noise. *Publ. Astron. Soc. Pacific* **121**, 414–427 (2009).
 22. Breiman, L. Random Forests. *Mach. Learn.* **45**, 5–32 (2001).
 23. Brocher, E.-C. The BioVoxel Image Processing and Analysis Toolbox. in *Eur. BioImage Anal. Symp., Paris* 336–338 (2013).
 24. Voigt, F. F. *et al.* The mesoSPIM initiative: open-source light-sheet microscopes for imaging cleared tissue. *Nat. Methods* **16**, 1105–1108 (2019).

25. Sharpe, J. *et al.* Optical projection tomography as a tool for 3D microscopy and gene expression studies. *Science (80-.)*. **296**, 541–545 (2002).
26. Nguyen, D. *et al.* Supervised learning to quantify amyloidosis in whole brains of an Alzheimer’s disease mouse model acquired with optical projection tomography. *Biomed. Opt. Express* **10**, 3041 (2019).
27. Govindan, S., Batti, L., Osterop, S. F., Stoppini, L. & Roux, A. Mass Generation, Neuron Labeling, and 3D Imaging of Minibrains. *Front. Bioeng. Biotechnol.* **8**, 1–17 (2021).
28. Bens, M. *et al.* Corticosteroid-dependent sodium transport in a novel immortalized mouse collecting duct principal cell line. *J. Am. Soc. Nephrol.* **10**, 923–924 (1999).
29. Hasler, U., Vinciguerra, M., Vandewalle, A., Martin, P. Y. & Féraille, E. Dual effects of hypertonicity on aquaporin-2 expression in cultured renal collecting duct principal cells. *J. Am. Soc. Nephrol.* **16**, 1571–1582 (2005).
30. Arganda-Carreras, I. *et al.* Trainable Weka Segmentation: A machine learning tool for microscopy pixel classification. *Bioinformatics* **33**, 2424–2426 (2017).
31. Renier, N. *et al.* IDISCO: A simple, rapid method to immunolabel large tissue samples for volume imaging. *Cell* **159**, 896–910 (2014).
32. Berg, S. *et al.* ilastik: interactive machine learning for (bio)image analysis. *Nat. Methods* **16**, 1226–1232 (2019).
33. Nguyen, D. *et al.* Optical projection tomography for rapid whole mouse brain imaging. *Biomed. Opt. Express* **8**, 5637 (2017).
34. Kak, A. C., Slaney, M. & Wang, G. Principles of Computerized Tomographic Imaging. *Med. Phys.* **29**, 107–107 (2002).
35. Schindelin, J. *et al.* Fiji: An open-source platform for biological-image analysis. *Nat. Methods* **9**, 676–682 (2012).

Supplementary Files

This is a list of supplementary files associated with this preprint. Click to download.

- [SIStatisticaldistortionofsupervisedlearningpredictionsinopticalmicroscopyinducedbyimageompression.pdf](#)